

## Revisiting the activity–rotation relation for evolved stars

HENGGENG HAN,<sup>1</sup> SONG WANG<sup>†,1,2</sup> XUE LI,<sup>1,3</sup> CHUANJIE ZHENG,<sup>1,3</sup> AND JIFENG LIU<sup>1,3,2,4</sup>

<sup>1</sup>*Key Laboratory of Optical Astronomy, National Astronomical Observatories, Chinese Academy of Sciences, Beijing 100101, People’s Republic of China*

<sup>2</sup>*Institute for Frontiers in Astronomy and Astrophysics, Beijing Normal University, Beijing, 102206, People’s Republic of China*

<sup>3</sup>*School of Astronomy and Space Science, University of Chinese Academy of Sciences, Beijing 100049, People’s Republic of China*

<sup>4</sup>*New Cornerstone Science Laboratory, National Astronomical Observatories, Chinese Academy of Sciences, Beijing, 100012, People’s Republic of China*

### ABSTRACT

The magnetic dynamo mechanism of giant stars remains an open question, which can be explored by investigating their activity–rotation relations with multiple proxies. By using the data from the LAMOST and *GALEX* surveys, we carried out a comprehensive study of activity–rotation relations of evolved stars based on Ca II H&K lines, H $\alpha$  lines and near ultraviolet (NUV) emissions. Our results show that evolved stars and dwarfs obey a similar power-law in the unsaturated region of the activity–rotation relation, indicating a common dynamo mechanism in both giant and dwarfs. There is no clear difference in the activity levels between red giant branch stars and red clump stars, nor between single giants and those in binaries. Additionally, our results show that the NUV activity levels of giants are comparable to those of G- and K-type dwarfs and are higher than those of M dwarfs.

*Unified Astronomy Thesaurus concepts:* Red giant clump (1370); Red giant stars (1372); Stellar activity (1580); Stellar rotation (1629);

### 1. INTRODUCTION

Stellar magnetic fields are generated and maintained by stellar rotation and turbulent motion, named magnetic dynamo (Parker 1955). Stellar chromospheric activities are mostly caused by the variation of their magnetic fields, thus chromospheric emissions are excellent tracers of stellar magnetic fields (Wilson 1978; Barden 1985). The widely used chromospheric activity indices including Ca II H&K lines, H $\alpha$  lines and ultraviolet (UV) fluxes, could map the activities of different layers of the chromosphere (Vernazza et al. 1981; Fontenla et al. 2015; Linsky 2017).

Magnetic activities were observed among late-type dwarfs across the Hertzsprung–Russell (HR) diagram. Pioneer works have suggested that there is a dividing-line in the HR diagram, which separates two distinct groups of stars, i.e., a solar-type group with detected magnetic activities and a non-solar-type group corresponding to cool giants, among which magnetic activities were not observed (Linsky & Haisch 1979; Ayres et al. 1981). However, later on, many studies have found

signals of magnetic activities from subgiants and giants (e.g. Baliunas et al. 1983; Simon & Drake 1989). Investigating the magnetic activity of evolved stars has gradually become an important topic.

As a star evolves it will gradually lose angular momentum and thus present weak magnetic activity (Skumanich 1972). However, recent researches have found many active evolved stars with small rotation periods (Gaulme et al. 2020; Gehan et al. 2022). Some of them are in close-in binaries and have been spun-up by tidal interaction of their companions (Tayar et al. 2015), while there is still a large fraction of them are single stars. The origin of magnetic activity presented on these stars is worth investigating.

One of the open questions regarding on stellar activity of giants is, could main sequence and evolved stars develop a similar stellar dynamo? Similar to dwarfs, the magnetic activities of giants have been found to be positively correlated to rotation velocity (e.g. Strassmeier et al. 1994). Recent works have found that main-sequence and evolved stars fall on the same rotation-activity sequence in the unsaturated regime (Lehtinen et al. 2020; Wang et al. 2020). However, their samples mainly contain subgiants. Dixon et al. (2020) pro-

<sup>†</sup> Corresponding Author: songw@bao.ac.cn

posed that for evolved stars, the NUV activity-rotation relation of evolved stars is similar to that of M dwarfs but have different slope in the decay region. Whether the evolved stars and dwarfs obey the same activity-rotation relation is still unclear, and a large sample of evolved star with multi-band observations is needed to revisit this question.

Nowadays there are many elite sky surveys including the *Kepler* mission (Koch et al. 2010), the *Galaxy Evolution Explorer* (*GALEX*) mission (Morrissey et al. 2007), and the Large Sky Area Multi-Object Fiber Spectroscopic Telescope (LAMOST)-*Kepler*/K2 projects (Fu et al. 2020), making it possible to carry out a comprehensive study of chromospheric activity of evolved stars. In this work, based on the catalog from Ceillier et al. (2017), which measured rotation periods for giant stars, we investigated stellar activity-rotation relations of evolved stars, including red giant branch (RGB) and red clump (RC) stars. This paper is organized as follows. Section 2 describes the sample construction and methods. Section 3 gives the results and discussions.

## 2. SAMPLE CONSTRUCTION AND METHODS

### 2.1. Sample construction

The *Kepler* mission (Koch et al. 2010) has provided us with roughly 200,000 light curves with high quality, based on which Ceillier et al. (2017) have measured rotation periods of 361 giants, including RGB and RC stars. Various contamination including pulsation and binarity have been excluded, making this sample an ideal one to study the relation between activity and rotation of evolved stars. We cross-matched the sample with LAMOST DR10 to obtain their spectra and stellar parameters (Cui et al. 2012; Luo et al. 2015). For targets with multiple observations, the spectrum with the highest signal-to-noise ratio and corresponding parameter estimation were used.

The revised *GALEX* catalog GR6+7 contains 292,296,11 targets with near ultraviolet (NUV) and far ultraviolet (FUV) observations (Bianchi et al. 2017). We also cross-matched the sample from Ceillier et al. (2017), which have LAMOST stellar parameters, with the *GALEX* catalog using a radius of 3". In order to avoid contamination, we removed targets with "nuv\_artifact" larger than one, which represents "NUV bright star window reflection", "dichroic reflection", "detector run proximity" or "bright star ghost". This led to 86 targets with UV observations. All the *GALEX* data could be found at MAST (STScI 2013).

Generally, giants are thought to have low magnetic activity levels. However, light curves from *Kepler* observations show that roughly 8% red giants exhibit ro-

tational modulation, suggesting notable magnetic activity (e.g. Gaulme et al. 2020). Meanwhile, the authors suggested that about 15% of these red giants belong to close-in binaries (according to their rotation periods), which may exhibit higher magnetic activity compared to single red giants. This enhancement may bias the activity-rotation relation for single stars.

Therefore, we took additional steps to identify potential binaries. First, we cross-matched the giant sample with LAMOST DR10 to obtain radial velocity (RV) values (Luo et al. 2015), and marked giants with RV variations larger than 10 km/s. Second, we cross-matched the giants with *Gaia* eDR3 and the None-Single Star (NSS) catalog (Gaia Collaboration et al. 2021), marking those with RUWE values larger than 1.4 or listed in the NSS catalog. Third, we checked the giants against the SIMBAD database, but none were marked as binaries. Therefore, we classified our sample into single stars and binaries.

Moreover, we cross-matched our sample with *Gaia* eDR3 catalog (Gaia Collaboration et al. 2021) to get *Gaia* *G*, *BP* and *RP* photometry. We adopted the *Gaia* eDR3 distances from Bailer-Jones et al. (2021). *B* band and *V* band photometry were extracted from the UCAC4 catalog (Zacharias et al. 2013). Finally, the interstellar reddening were derived based on the Pan-STARRS1 3D dust map (Green 2018; Green et al. 2019).

### 2.2. LAMOST spectra

LAMOST is a reflecting Schmidt telescope, with an aperture of 3.6 to 4.9 m and a field of view of 5 degrees (Cui et al. 2012). Two kinds of spectra with different resolution have been provided. One is the low-resolution spectra with a resolution of  $R \sim 1800$ , the other is the medium-resolution spectra with a resolution of  $R \sim 7500$ . The low-resolution spectra cover a wavelength range of 3700–9000 Å, while the median-resolution spectra have a wavelength coverage of 4950–5350 Å at the blue arm and 6300–6800 Å at the red arm (Fu et al. 2020). Since we focused on both the Ca II H&K and H $\alpha$  lines, we used the low-resolution spectra in this work.

Before the calculation of activity indices, we corrected the RVs of the spectra using the RV values provided by the LAMOST DR10 catalog (Luo et al. 2015). Meanwhile, we used the smoothing spline method from the *laspec* package (Zhang et al. 2020a) to normalize the LAMOST spectra. Figure 1 shows some examples of normalized spectra, the Ca II H&K and H $\alpha$  lines and corresponding continua. To guarantee the quality of LAMOST spectra, in following analysis we excluded those with a signal-to-noise ratio lower than 30.

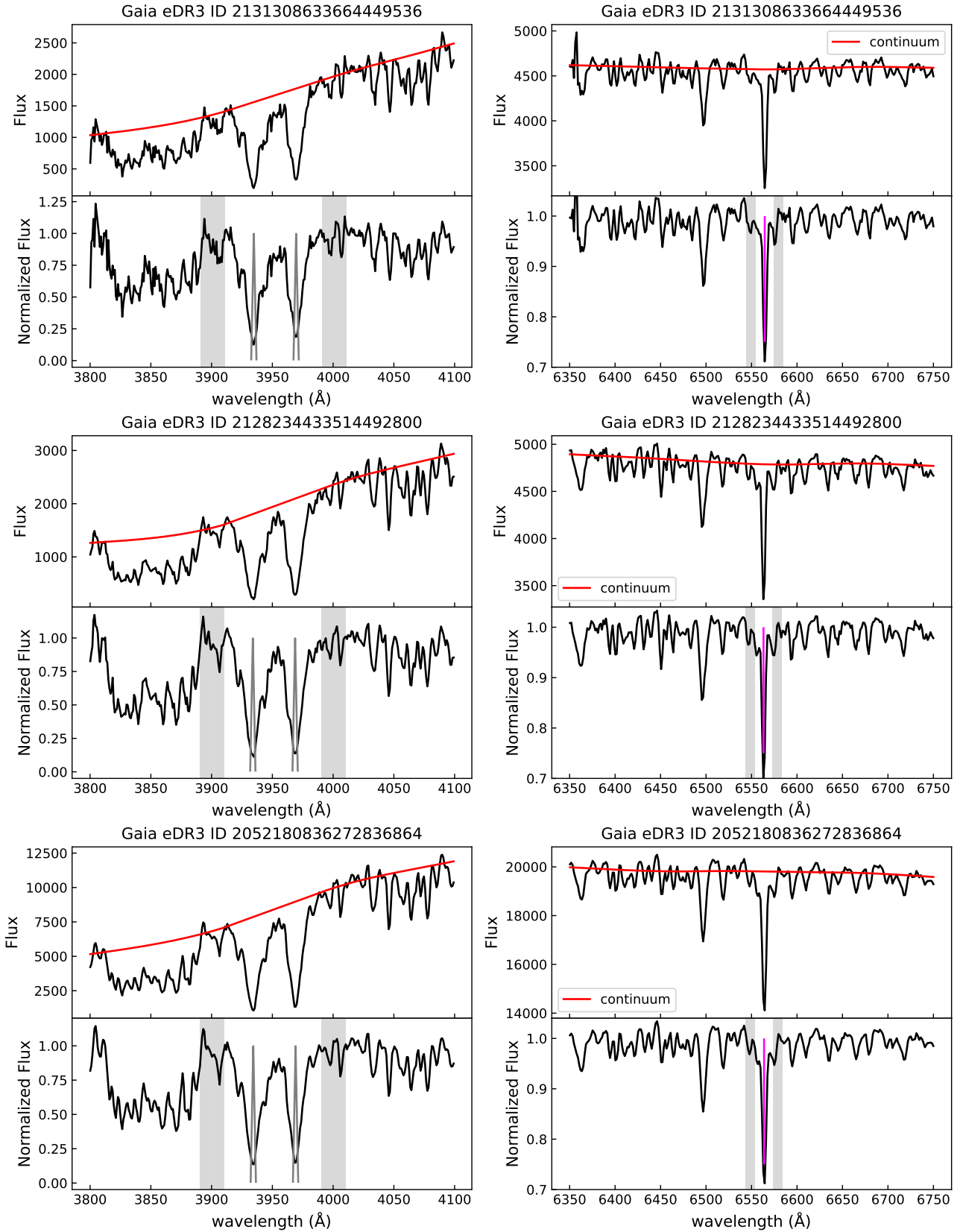


**Figure 1.** Left panels: Examples of LAMOST blue-band spectra and their normalization. Red lines are continua used for normalization. Grey shaded areas mark the continua used for the calculation of  $S_{\text{LAMOST}}$  using the Ca II H&K lines. Grey triangles are integration windows of Ca II H&K lines with an FWHM of 2.18 Å. Right panels: Examples of LAMOST red-band spectra and their normalization. Grey shaded areas mark the continua used for the calculation of  $EW_{\text{H}\alpha}$  using H $\alpha$  lines. Magenta lines mark the RV-corrected line centers of H $\alpha$  lines.

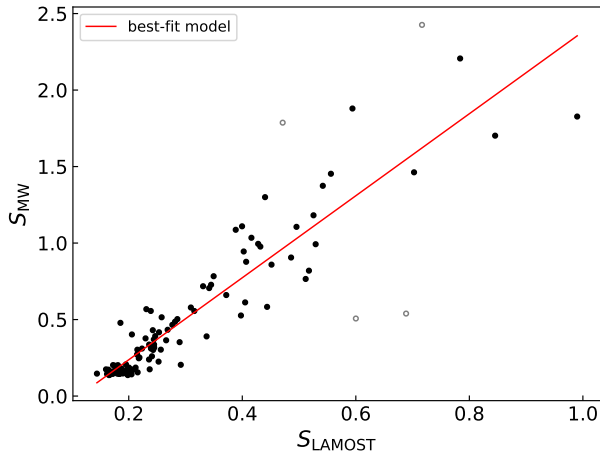


**Figure 2.** Relation between  $S_{\text{LAMOST}}$  and  $S_{\text{MW}}$ . The red line represents the best-fit model. The gray open circles are not included in the fitting.

### 2.3. Rotation periods and Rossby number

As discussed above, we used the rotation periods estimated from *Kepler* data (Ceillier et al. 2017). Considering that the *Kepler* satellite would rotate 90 degrees every 90 days (Van Cleve & Caldwell 2016), which could cause systematic variability and contaminate light curves, we removed all the targets with rotation periods between 85 days and 95 days.

To calculate the Rossby number ( $\text{Ro} = P_{\text{rot}}/\tau_c$ ), we further calculated the convective turnover time ( $\tau_c$ ) using the Yale-Potsdam Stellar Isochrones (YAPSI; Spada et al. 2017). The subgrids that contain solar calibration were adopted. First, we calculated the bolometric luminosity of our sample,  $L_{\text{bol}} = 10^{-0.4 \times (m_\lambda - 5 \log_{10} d + 5 - A_\lambda + BC_\lambda - M_\odot)} L_\odot$ , in *G*, *BP*, *RP*, *J*, *H* and *Ks* bands. Here  $M_\odot = 4.74$  mag is the solar bolometric magnitude and  $L_\odot = 3.828 \times 10^{33}$  erg/s is the solar bolometric luminosity. We used the mean and standard deviation of  $L_{\text{bol}}$  corresponding to six bands as the final  $L_{\text{bol}}$  and its error. Second, for each target, the metallicity grid closest to the observed  $[\text{Fe}/\text{H}]$  was chosen and the models within the typical errors of  $T_{\text{eff}}$  and  $\log L_{\text{bol}}$  were picked out, which were set to be 200 K and 0.2, respectively. We then calculated the median value of  $\tau_c$  with these models as the final  $\tau_c$ .

### 2.4. Activity indices

#### 2.4.1. Ca II H&K index: $R'_{\text{HK}}$

Known as the Wilson-Bappu effect, the widths of the emission cores of Ca II H&K lines would increase towards higher luminosities, especially for evolved stars (Wilson & Vainu Bappu 1957). Consequently, the Mount Wilson Observatory (MWO) used a 2 Å slit to estimate the

fluxes of the Ca II H&K lines of giant stars (Duncan et al. 1991). Recently, this effect has been revisited by Schröder et al. (2018) to illustrate that when calculating *S*-index using the data from spectra, a wider integration window is also needed for giants.

To quantify the strength of Ca II H&K lines, we first calculated the *S*-index using the normalized LAMOST spectra:

$$S_{\text{LAMOST}} = 8 \cdot \alpha \cdot \frac{H + K}{R + V}. \quad (1)$$

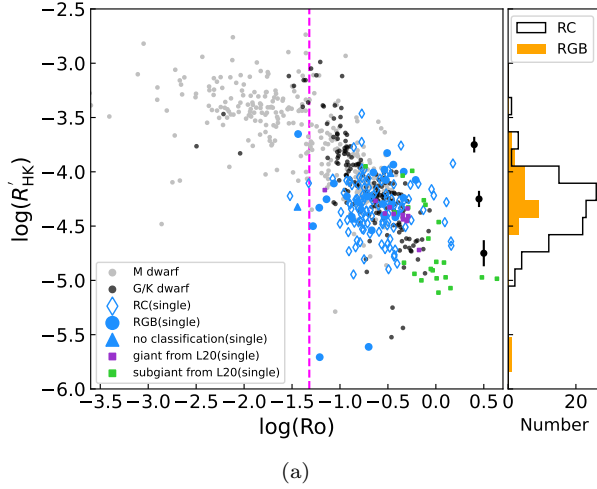
Unlike previous studies which used an integration window with a full width at half maximum (FWHM) of 1.09 Å (e.g. Karoff et al. 2016; Zhang et al. 2020b), in this work, we used a triangle bandpass with an FWHM of 2.18 Å, consistent with observations of the MWO. *H* and *K* are the integrated flux in the triangle bandpass centered at 3969.59 Å and 3934.78 Å, respectively, as shown in Figure 1 (left panels). *R* and *V* represent the integrated flux in the 20 Å rectangle windows (shaded areas in panel (a) of Figure 1) centered at 4001 Å and 3901 Å, respectively. The  $\alpha$  was set to be 1.8 according to Hall et al. (2007). The factor 8 accounts for the different exposing strategies of different channels of Mount Wilson spectrophotometer. In order to derive the error of  $S_{\text{LAMOST}}$ , for each target, 1000 synthetic spectra were simulated based on the Gaussian noise at each wavelength. We then calculated  $S_{\text{LAMOST}}$  of each spectrum and used their standard deviation as the error of  $S_{\text{LAMOST}}$ .

To convert  $S_{\text{LAMOST}}$  to the well-known Mount Wilson *S*-index ( $S_{\text{MW}}$ ), we cross-matched the sample from Boro Saikia et al. (2018) with LAMOST DR10 and a linear model was fitted to the common targets using the least squares:

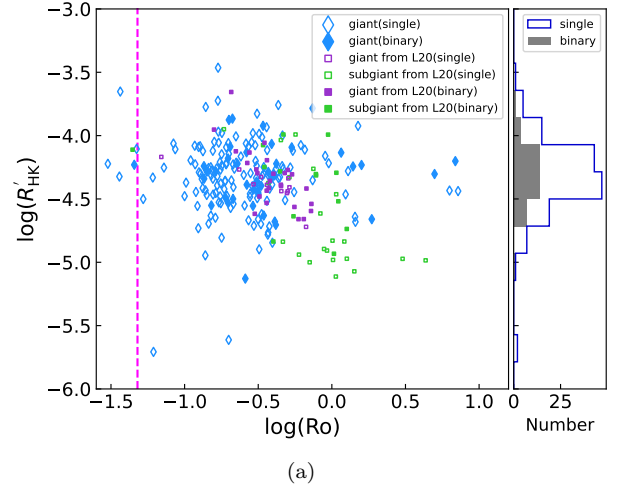
$$S_{\text{MW}} = a \times S_{\text{LAMOST}} + b, \quad (2)$$

where  $a = 2.68 \pm 0.23$  and  $b = -0.3 \pm 0.06$  (Figure 2). To estimate the uncertainty of the linear fitting, we repeated the fitting process 10,000 times through random sampling the errors in  $S_{\text{LAMOST}}$ . The standard deviations of the 10,000 values of  $a$  and  $b$  were then used as the uncertainties of  $a$  and  $b$ , respectively. These uncertainties were subsequently incorporated into the errors of  $R'_{\text{HK}}$  through error propagation.

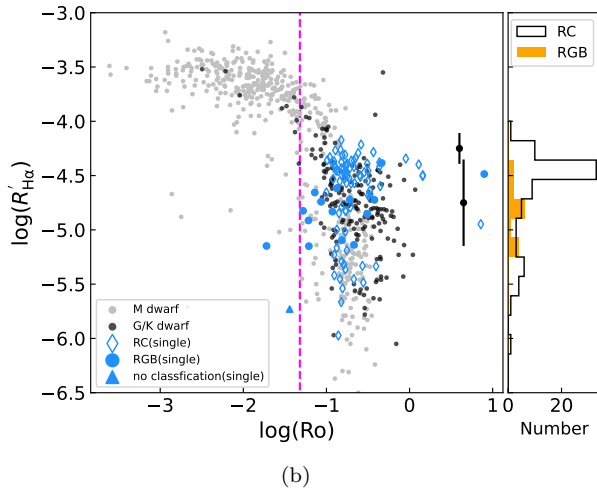
It is important to note that the common sources between LAMOST DR10 and Boro Saikia et al. (2018) are all dwarfs, and their  $S_{\text{LAMOST}}$  values were estimated using a triangle bandpass with a typical FWHM of 1.09 Å. We assumed that the conversion derived from dwarfs is also applicable for giants, whose  $S_{\text{LAMOST}}$  values were estimated using a triangle bandpass with an FWHM of 2.18 Å, this assumption may introduce some uncertainties.



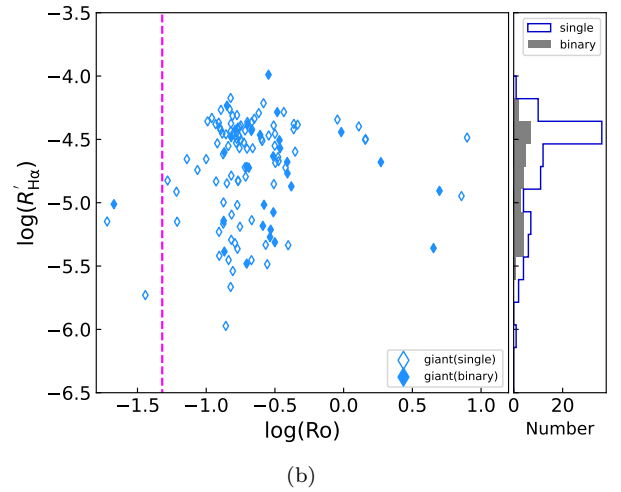
(a)



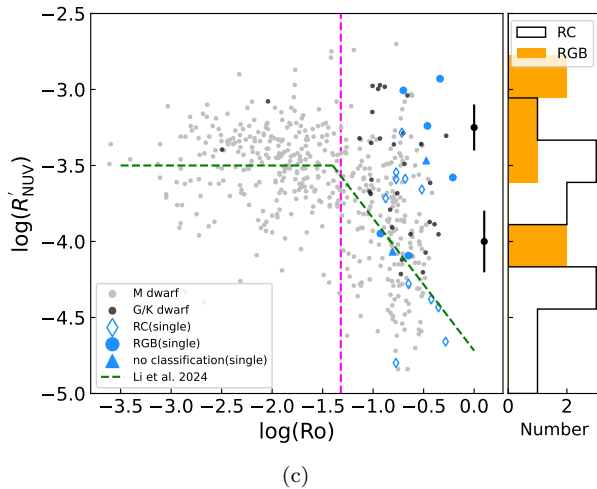
(a)



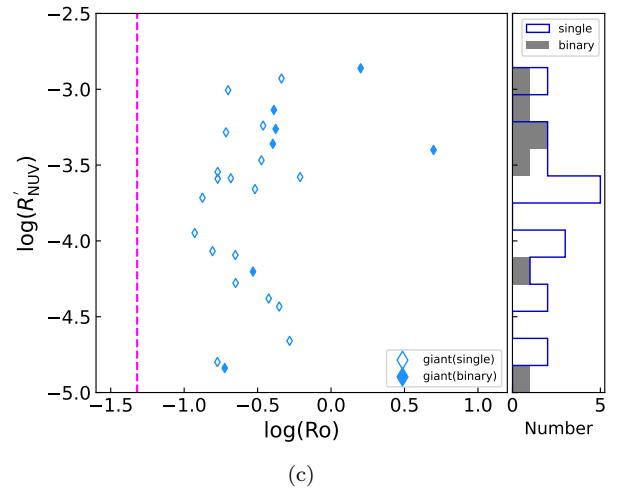
(b)



(b)



(c)



(c)

**Figure 3.** Activity–rotation relations for single stars including  $R'_{\text{HK}}-\text{Ro}$  relation (Panel (a)),  $R'_{\text{H}\alpha}-\text{Ro}$  relation (Panel (b)), and  $R'_{\text{NUV}}-\text{Ro}$  relation (Panel (c)). The black segments represent typical errors of activity indices for giants at different activity levels. The magenta lines mark the knee point,  $\log(\text{Ro}) = -1.32$ , separating the saturated and the unsaturated regimes from Han et al. (2024). The green dashed line is the fitting result for M dwarfs from Li et al. (2024).

**Figure 4.** Activity–rotation relations of single and binary evolve stars, including  $R'_{\text{HK}}-\text{Ro}$  relation (Panel (a)),  $R'_{\text{H}\alpha}-\text{Ro}$  relation (Panel (b)), and  $R'_{\text{NUV}}-\text{Ro}$  relation (Panel (c)). The magenta lines mark the knee point,  $\log(\text{Ro}) = -1.32$ , separating the saturated and the unsaturated regimes from Han et al. (2024).

Finally, in order to get the pure chromospheric activity, the contribution of photosphere and dependence on spectral type of  $S$ -index need to be corrected (Noyes et al. 1984). We then followed the approach of Linsky et al. (1979):

$$R'_{\text{HK}} = \frac{\mathcal{F}_{\text{HK}} - \mathcal{F}_{\text{HK,ph}}}{\sigma T_{\text{eff}}^4}, \quad (3)$$

where  $\mathcal{F}_{\text{HK}}$  is total flux of Ca II H&K lines, which was calculated as  $\mathcal{F}_{\text{HK}} = S_{\text{MW}} \cdot \mathcal{F}_{\text{RV}}/8\alpha$  according to Middekoop (1982). Following Mittag et al. (2013), here  $\alpha = 2.4$ .  $\mathcal{F}_{\text{RV}}$  is the total flux in the  $R$  and  $V$  windows. For dwarfs with  $B - V$  between 0.44 and 1.6,  $\mathcal{F}_{\text{RV}} = 19.2 \times 10^{8.25-1.67(B-V)}$ . For giants with  $B - V$  between 0.76 and 1.18,  $\mathcal{F}_{\text{RV}} = 19.2 \times 10^{8.33-1.79(B-V)}$ .  $\mathcal{F}_{\text{HK,ph}}$  is the contribution of photosphere to the Ca II H&K lines. For dwarfs with  $B - V$  between 0.44 and 1.28, 1.28 and 1.6,  $\mathcal{F}_{\text{HK,ph}} = 10^{7.49-2.06(B-V)}$  and  $\mathcal{F}_{\text{HK,ph}} = 10^{6.19-1.04(B-V)}$ , respectively. While for giants with  $B - V$  between 0.76 and 1.18,  $\mathcal{F}_{\text{HK,ph}} = 10^{7.61-2.37(B-V)}$ . Here  $B - V$  is the intrinsic color.  $\sigma$  is the Stefan-Boltzmann constant and  $T_{\text{eff}}$  is the effective temperature. The errors of  $S_{\text{MW}}$  were derived through the error propagation of  $S_{\text{LAMOST}}$  errors. Then errors of  $R'_{\text{HK}}$  were estimated through random sampling of errors of  $S_{\text{MW}}$  and  $T_{\text{eff}}$ .

#### 2.4.2. H $\alpha$ index: $R'_{\text{H}\alpha}$

Following Han et al. (2023), we calculated the H $\alpha$  activity index  $R'_{\text{H}\alpha}$ . First, the equivalent widths of H $\alpha$  lines were defined as

$$EW = \int \frac{F_c - F_\lambda}{F_c} d\lambda. \quad (4)$$

The integration interval was set to be 20 Å centered at 6564.6 Å. The  $F_c$  was defined as the median value of pseudo-continua (shaded areas in panel (b) of Figure 1). Similar to the Ca II H&K lines, the photospheric contribution to the H $\alpha$  lines needs to be subtracted:

$$EW' = EW - EW_{\text{ph}}, \quad (5)$$

where  $EW_{\text{ph}}$  was estimated using Eq. (4) based on PHOENIX synthetic spectra (Husser et al. 2013) with the closest  $T_{\text{eff}}$ , surface gravity ( $\log g$ ) and metallicity ([Fe/H]) to our giant sample.

Then, following Walkowicz et al. (2004) we converted  $EW'$  to normalized H $\alpha$  luminosity:

$$R'_{\text{H}\alpha} = L_{\text{H}\alpha}/L_{\text{bol}} = \chi \cdot EW'. \quad (6)$$

The factor  $\chi$  was calculated as

$$\chi = \frac{f_{\lambda 6564}}{\sigma T_{\text{eff}}^4}. \quad (7)$$

$f_{\lambda 6564}$  is the continuum flux at 6564 Å, which was estimated through fitting the continuum of PHOENIX spectra (Husser et al. 2013) with nearest stellar parameters to our giant sample. The error of  $EW$  was calculated with similar steps to  $S_{\text{LAMOST}}$ . The error of  $R'_{\text{H}\alpha}$  was estimated using error propagation of  $EW$ .

#### 2.4.3. NUV index: $R'_{\text{NUV}}$

To quantify NUV activity level, we calculated the  $R'_{\text{NUV}}$  index following Li et al. (2024):

$$R'_{\text{NUV}} = \frac{f_{\text{NUV,obs}} \cdot \left(\frac{d}{R}\right)^2 - f_{\text{NUV,ph}}}{\sigma T_{\text{eff}}^4}. \quad (8)$$

Here  $f_{\text{NUV,obs}}$  is the observed NUV flux with interstellar reddening being corrected:

$$f_{\text{NUV,obs}} = 10^{-0.4 \cdot (m_{\text{NUV}} - 20.08 - R_{\text{NUV}} \cdot E(B-V))} \times \delta\lambda_{\text{NUV}} \times 2.06 \times 10^{-16}. \quad (9)$$

$f_{\text{NUV,ph}}$  is the photospheric contribution to the NUV flux.  $R_{\text{NUV}} = 8.71$  is the NUV extinction coefficients (Cardelli et al. 1989). In this work, we applied the PARSEC evolutionary tracks (Bressan et al. 2012) with metallicity grids of  $-2.5$ ,  $-2.0$ ,  $-1.5$ ,  $-1.0$ ,  $-0.5$ ,  $0.0$ ,  $0.3$ ,  $0.5$ ,  $1.0$  to estimate the photospheric contribution in NUV band. For each target, we first selected two model grids with the closest metallicity. Then, we extracted the best model by comparing the theoretical and observed  $T_{\text{eff}}$  and  $L_{\text{bol}}$  to get the photospheric NUV magnitude, which was further converted to  $f_{\text{NUV,ph}}$ . Finally, we obtained the final  $f_{\text{NUV,ph}}$  by linear interpolation using metallicity. In Eq. (9),  $\delta\lambda_{\text{NUV}}$  is the effective bandwidth of 1060 Å and  $R_{\text{NUV}}$  is the extinction coefficient in NUV band from Fitzpatrick (1999).  $d$  is the Gaia eDR3 distance (Bailer-Jones et al. 2021). Stellar radius  $R$  was calculated as

$$R = \sqrt{\frac{L_{\text{bol}}}{4\pi\sigma T_{\text{eff}}^4}} = \sqrt{\frac{10^{-0.4 \times (m_\lambda - 5 \log_{10} d + 5 - A_\lambda + BC_\lambda - M_\odot)} L_\odot}{4\pi\sigma T_{\text{eff}}^4}}.$$

$m_\lambda$ ,  $A_\lambda$ ,  $BC_\lambda$  are the apparent magnitude, extinction, defined as  $R_\lambda \cdot E(B - V)$ , and bolometric correction in different bands. We used the *isochrones* package (Morton 2015) to derive the  $BC_\lambda$  based on stellar parameters including  $T_{\text{eff}}$ ,  $\log g$  and [Fe/H]. The calculation was repeated for  $G$ ,  $BP$ ,  $RP$ ,  $J$ ,  $H$  and  $Ks$  bands. We used the mean value and standard deviation of  $R$  in six bands as the final stellar radius and its error, respectively. The error of  $R'_{\text{NUV}}$  was estimated using the sampling of errors of  $f_{\text{NUV}}$ , distance, radius and  $T_{\text{eff}}$ .

### 3. RESULTS AND DISCUSSIONS

Stellar activity–rotation relations of dwarfs have been extensively studied. To construct activity–rotation relations of evolved stars and compare them to those of

dwarfs, we first gathered samples from Li et al. (2024) and Han et al. (2023), which mainly contain M-, K- and G-type dwarfs with measured Ro and chromospheric activity indices. To get unified Ca II H&K activity index, we re-calculated the  $R'_{\text{HK}}$  of these samples using the methods described in Section 2.4.1, but with an integration window of 1.09 Å for the Ca II H&K lines. We also cross-matched dwarfs from Han et al. (2023) with the *GALEX* GR6+7 catalog using a radius of 3" and calculated  $R'_{\text{NUV}}$  of those with NUV detection following Section 2.4.3. Meanwhile, we directly gathered  $R'_{\text{H}\alpha}$  and  $R'_{\text{NUV}}$  values of dwarf stars from these studies.

Finally, we got 181, 125, and 27 giants with  $R'_{\text{HK}}$ ,  $R'_{\text{H}\alpha}$  and  $R'_{\text{NUV}}$  measurements, respectively. In addition, we cross-matched our giant sample with the catalog from Wang et al. (2023) to distinguish between red giant branch (RGB) and red clump (RC) stars. Our sample includes 163 RC stars, 40 RGB stars, and 7 giants without classification. The final results together with stellar parameters are presented in Table 1.

Late type stars have convective envelope and radiative core and thus could develop a solar-like dynamo, i.e.,  $\alpha - \Omega$  dynamo (Parker 1955). As a result, the well-known activity-rotation relations could act as diagnostics of stellar dynamos. For dwarfs, various chromospheric indices including Ca II H&K lines, H $\alpha$  lines and NUV emissions follow a similar relation, including a saturated region and a decay region. (e.g. Noyes et al. 1984; Wright et al. 2011; Newton et al. 2016). In this work, we built activity-rotation relations for both dwarfs and evolved stars (Figure 3).

In the  $R'_{\text{HK}}$ -Ro relation (Figure 3) we also included sample from Lehtinen et al. (2020). Their  $S_{\text{MW}}$  values were converted to  $R'_{\text{HK}}$  using the method in Section 2.4.1. In addition, we removed targets flagged with "likely spurious  $P_{\text{rot}}$ " and "unreliable  $\tau_c$ " by Lehtinen et al. (2020). We also classified their sample into single stars and binaries using following steps. We cross-matched their sample with Gaia eDR3 and the NSS catalog, and selected those with RUWE values larger than 1.4 or listed in the NSS catalog. Furthermore, by cross-matching with SIMBAD, we identified sources marked as spectroscopic binaries or RS Canum Venaticorum variables. Most of the remaining single stars from Lehtinen et al. (2020) are subgiants, which follows a similar  $R'_{\text{HK}}$ -Ro relation as dwarfs.  $R'_{\text{HK}}$  values of giants exhibit some scatter, which is expected given that either stellar activity or the  $B - V$  color can vary, with the latter could influence the calculation of the photospheric Ca II H&K flux. We remind that the  $S$ -index of evolved stars in both our sample and Lehtinen et al. (2020) was calculated with a 2 Å window, while the photospheric

contribution to the Ca II H&K lines was estimated using a 1 Å window following Mittag et al. (2013). This may overestimate the  $R'_{\text{HK}}$  values of giant stars.

All the RGB stars, RC stars, and dwarfs fall on a single sequence in the unsaturated regime, and we did not observe a separation between the RGB stars and RC stars in any of the three activity-rotation relations. We also found that, giants exhibit NUV activity levels similar to those of G and K dwarfs. Although some giants show higher levels compared to M dwarfs, the difference is not as significant as reported by Dixon et al. (2020), who reported that the relationship between NUV excess and the Rossby number for evolved stars follows a similar trend to that seen in M dwarfs, but with different slope. We propose that in evolved stars, the magnetic field is also generated by both convection and rotation, suggesting a shared dynamo mechanism between giants and dwarfs.

Figure 4 shows a comparison between single and binary evolved stars. We did not find clear difference in magnetic activity levels between single stars and binaries, suggesting that the magnetic activity of these binaries is dominated by the giant component. This is not unexpected, as most of these giants in binaries have long periods (i.e., rotational or orbital). Therefore, we do not observe the results like that giants in close binaries exhibit significantly higher activity levels than single giants, since their rotation rates may have been greatly increased due to tidal interactions with their companions (Gehan et al. 2022).

#### 4. SUMMARY

In this study, based on data from the LAMOST and *GALEX* sky surveys, together with the catalog from Ceillier et al. (2017), which estimated rotation periods of evolved stars, we investigated the activity-rotation relations for evolved stars using the  $R'_{\text{HK}}$ ,  $R'_{\text{H}\alpha}$ , and  $R'_{\text{NUV}}$  indices.

We found that, for all these three activity indices, evolved stars and dwarfs obey a similar power-law in the unsaturated region of activity-rotation relations, indicating a shared dynamo mechanism in giant and dwarfs. Our results generally show that the NUV activity levels of giants are comparable to those of G- and K-type dwarfs and are higher than those of M dwarfs. However, the difference is not as significant as reported by Dixon et al. (2020). Additionally, we did not find significant difference in the activity levels between RC stars and RGB stars.

Furthermore, there is no clear difference in the activity levels between single and binary evolved stars, indicating that the magnetic activity in binaries is dominated

**Table 1.** Stellar parameters of and activity proxies of evolved stars in our sample.

Gaia ID	R.A.	Decl.	$T_{\text{eff}}$	$\log g$	[Fe/H]	$\log R'_{\text{HK}}$	$\log R'_{\text{H}\alpha}$	$\log R'_{\text{NUV}}$	$P_{\text{rot}}$	$\tau_c$	flag
(1)	(degree)	(degree)	(K)	(dex)	(dex)	(7)	(8)	(9)	(day)	(day)	(11)
2050241224731793408	291.35999	36.81989	4835±27	2.47±0.04	-0.45±0.02	-4.55±0.09	-4.48±0.08	-	46.74	307.54	RC/b
2051086822197774464	290.51929	37.52545	4852±35	2.4±0.05	-0.5±0.03	-4.08±0.07	-4.42±0.06	-	40.98	321.54	RC/s
2051739416708443392	292.16775	37.39372	4775±41	2.5±0.06	-0.34±0.04	-4.31±0.19	-4.37±0.63	-	44.54	293.96	RC/s
2076974033203960448	297.30347	42.02882	5122±36	3.05±0.05	0.1±0.03	-4.24±0.06	-	-2.93±0.6	103.74	225.71	RGB/s
2087245121068056064	297.54099	49.86628	5035±28	2.96±0.04	0.17±0.02	-4.33±0.07	-4.6±0.09	-4.43±1.18	97.47	219.64	RC/s
2101726238962567552	291.22244	41.82693	4713±26	2.8±0.04	-0.14±0.02	-4.23±0.1	-4.83±0.65	-3.95±1.16	41.27	349.67	RGB/s
2102112339341027840	288.37677	40.94816	4939±40	3.56±0.07	0.22±0.04	-5.61±8.26	-	-3.01±0.08	62.11	311.86	RGB/s
2102592478023537536	287.93837	42.92124	4901±20	3.03±0.03	0.29±0.01	-4.2±0.07	-	-3.66±0.12	120.88	398.25	RC/s
2105404311512378496	282.38805	44.41601	4774±22	2.44±0.03	-0.42±0.01	-4.63±0.09	-4.57±0.07	-	101.64	294.93	RC/b
2125777987100768512	291.77075	42.56832	4948±13	2.79±0.02	-0.01±0.01	-4.01±0.07	-4.67±0.12	-3.47±0.4	134.98	402.13	-/s
...	...	...	...	...	...	...	...	...	...	...	...

NOTE. (1) Gaia ID: Gaia eDR3 source ID. (2) R.A.: right ascension (3) Decl.: declination. (4)  $T_{\text{eff}}$ : effective temperature. (5)  $\log g$ : surface gravity. (6) [Fe/H]: metallicity. (7)  $\log R'_{\text{HK}}$ : Ca II H&K proxy. (8)  $\log R'_{\text{H}\alpha}$ : H $\alpha$  proxy. (9)  $\log R'_{\text{NUV}}$ : NUV proxy. (10)  $P_{\text{rot}}$ : rotation period. (11)  $\tau_c$ : convective turnover time. (12) flag: evolutionary stage. Single stars are marked by 's', potential binaries are marked by 'b'.

by the giant component. This is unsurprising, as most of the binaries in our sample are not close-in systems based on their periods, with tidal interactions too weak to enhance magnetic activity.

It is important to note that our  $R'_{\text{HK}}$  values for giants are based on the  $S$ -index calculated using a 2.18 Å triangle integration window, following the method of the MWO and accounting for the Wilson-Bappu effect, which suggests that the widths of the emission cores of the Ca II H&K lines increase with stellar luminosity. For dwarfs, however, the  $S$ -index was still calculated using a 1.09 Å window. No corrections were made for the differences in integration windows, which may introduce some uncertainties.

#### ACKNOWLEDGMENTS

We thank the referee for the comprehensive and useful comments. The Guoshoujing Telescope (the Large Sky Area Multi-Object Fiber Spectroscopic Telescope LAMOST) is a National Major Scientific Project built by the Chinese Academy of Sciences. Funding for the project has been provided by the National Development and Reform Commission. LAMOST is operated and managed by the National Astronomical Observatories, Chinese Academy of Sciences. Some of the data presented in this paper were obtained from the Mikulski Archive for Space Telescopes (MAST). This work presents results from the European Space Agency (ESA) space mission *Gaia*. *Gaia* data are being processed by the *Gaia* Data Processing and Analysis Consortium (DPAC). Funding for the DPAC is provided by national institutions, in particular the institutions participating in the *Gaia* MultiLateral Agreement (MLA). The *Gaia* mission website is <https://www.cosmos.esa.int/gaia>. The *Gaia* archive website is <https://archives.esac.esa.int/gaia>. We acknowledge use of the VizieR catalog access tool, operated at CDS, Strasbourg, France. This work was supported by National Key Research and Development Program of China (NKRDP) under grant No. 2019YFA0405000, Science Research Grants from the China Manned Space Project with No. CMS-CSST-2021-A08, Strategic Priority Program of the Chinese Academy of Sciences under grant No. XDB4100000, and National Natural Science Foundation of China (NSFC) under grant Nos. 11988101/11933004/11833002/12090042/12273057.



## REFERENCES

- Ayres, T. R., Linsky, J. L., Vaiana, G. S., Golub, L., & Rosner, R. 1981, *ApJ*, 250, 293
- Bailer-Jones, C. A. L., Rybizki, J., Fouesneau, M., Demleitner, M., & Andrae, R. 2021, *AJ*, 161, 147
- Baliunas, S. L., Hartmann, L., & Dupree, A. K. 1983, *ApJ*, 271, 672
- Barden, S. C. 1985, *ApJ*, 295, 162
- Bianchi, L., Shiao, B., & Thilker, D. 2017, *ApJS*, 230, 24
- Boro Saikia, S., Marvin, C. J., Jeffers, S. V., et al. 2018, *A&A*, 616, A108
- Bressan, A., Marigo, P., Girardi, L., et al. 2012, *MNRAS*, 427, 127
- Cardelli, J. A., Clayton, G. C., & Mathis, J. S. 1989, *ApJ*, 345, 245
- Ceillier, T., Tayar, J., Mathur, S., et al. 2017, *A&A*, 605, A111
- Cui, X.-Q., Zhao, Y.-H., Chu, Y.-Q., et al. 2012, *Research in Astronomy and Astrophysics*, 12, 1197
- Dixon, D., Tayar, J., & Stassun, K. G. 2020, *AJ*, 160, 12
- Duncan, D. K., Vaughan, A. H., Wilson, O. C., et al. 1991, *ApJS*, 76, 383
- Fitzpatrick, E. L. 1999, *PASP*, 111, 63
- Fontenla, J. M., Stancil, P. C., & Landi, E. 2015, *ApJ*, 809, 157
- Fu, J.-N., Cat, P. D., Zong, W., et al. 2020, *Research in Astronomy and Astrophysics*, 20, 167
- Gaia Collaboration, Brown, A. G. A., Vallenari, A., et al. 2021, *A&A*, 649, A1
- Gaulme, P., Jackiewicz, J., Spada, F., et al. 2020, *A&A*, 639, A63
- Gehan, C., Gaulme, P., & Yu, J. 2022, *A&A*, 668, A116
- Green, G. 2018, *The Journal of Open Source Software*, 3, 695
- Green, G. M., Schlafly, E., Zucker, C., Speagle, J. S., & Finkbeiner, D. 2019, *ApJ*, 887, 93
- Hall, J. C., Lockwood, G. W., & Skiff, B. A. 2007, *AJ*, 133, 862
- Han, H., Wang, S., Bai, Y., et al. 2023, *ApJS*, 264, 12
- Han, H., Wang, S., Zheng, C., et al. 2024, *ApJS*, 273, 8
- Husser, T. O., Wende-von Berg, S., Dreizler, S., et al. 2013, *A&A*, 553, A6
- Karoff, C., Knudsen, M. F., De Cat, P., et al. 2016, *Nature Communications*, 7, 11058
- Koch, D. G., Borucki, W. J., Basri, G., et al. 2010, *ApJL*, 713, L79
- Lehtinen, J. J., Spada, F., Käpylä, M. J., Olsper, N., & Käpylä, P. J. 2020, *Nature Astronomy*, 4, 658
- Li, X., Wang, S., Han, H., et al. 2024, *ApJ*, 966, 69
- Linsky, J. L. 2017, *ARA&A*, 55, 159
- Linsky, J. L., & Haisch, B. M. 1979, *ApJL*, 229, L27
- Linsky, J. L., Worden, S. P., McClintock, W., & Robertson, R. M. 1979, *ApJS*, 41, 47
- Luo, A. L., Zhao, Y.-H., Zhao, G., et al. 2015, *Research in Astronomy and Astrophysics*, 15, 1095
- Middelkoop, F. 1982, *A&A*, 113, 1
- Mittag, M., Schmitt, J. H. M. M., & Schröder, K. P. 2013, *A&A*, 549, A117
- Morrissey, P., Conrow, T., Barlow, T. A., et al. 2007, *ApJS*, 173, 682
- Morton, T. D. 2015, isochrones: Stellar model grid package, Astrophysics Source Code Library, record ascl:1503.010
- Newton, E. R., Irwin, J., Charbonneau, D., et al. 2016, *ApJ*, 821, 93
- Noyes, R. W., Hartmann, L. W., Baliunas, S. L., Duncan, D. K., & Vaughan, A. H. 1984, *ApJ*, 279, 763
- Parker, E. N. 1955, *ApJ*, 122, 293
- Schröder, K. P., Schmitt, J. H. M. M., Mittag, M., Gómez Trejo, V., & Jack, D. 2018, *MNRAS*, 480, 2137
- Simon, T., & Drake, S. A. 1989, *ApJ*, 346, 303
- Skumanich, A. 1972, *ApJ*, 171, 565
- Spada, F., Demarque, P., Kim, Y. C., Boyajian, T. S., & Brewer, J. M. 2017, *ApJ*, 838, 161
- Strassmeier, K. G., Handler, G., Paunzen, E., & Rauth, M. 1994, *A&A*, 281, 855
- STScI. 2013, GALEX/MCAT
- Tayar, J., Ceillier, T., García-Hernández, D. A., et al. 2015, *ApJ*, 807, 82
- Van Cleve, J. E., & Caldwell, D. A. 2016, Kepler Instrument Handbook, Kepler Science Document KSCI-19033-002, id.1. Edited by Michael R. Haas and Steve B. Howell
- Vernazza, J. E., Avrett, E. H., & Loeser, R. 1981, *ApJS*, 45, 635
- Walkowicz, L. M., Hawley, S. L., & West, A. A. 2004, *PASP*, 116, 1105
- Wang, C., Huang, Y., Zhou, Y., & Zhang, H. 2023, *A&A*, 675, A26
- Wang, S., Bai, Y., He, L., & Liu, J. 2020, *ApJ*, 902, 114
- Wilson, O. C. 1978, *ApJ*, 226, 379
- Wilson, O. C., & Vainu Bappu, M. K. 1957, *ApJ*, 125, 661
- Wright, N. J., Drake, J. J., Mamajek, E. E., & Henry, G. W. 2011, *ApJ*, 743, 48
- Zacharias, N., Finch, C. T., Girard, T. M., et al. 2013, *AJ*, 145, 44
- Zhang, B., Liu, C., & Deng, L.-C. 2020a, *ApJS*, 246, 9
- Zhang, J., Bi, S., Li, Y., et al. 2020b, *ApJS*, 247, 9